Origin of Efficient Inverted Nonfullerene Organic Solar Cells

Wang, Yiwen; Wu, Bo; Wu, Zhenghui; Lan, Zhaojue; Li, Yongfang; Zhang, Maojie; ZHU, Fu Rong

Published in:
Journal of Physical Chemistry Letters

DOI:
10.1021/acs.jpclett.7b02308

Published: 02/11/2017

Document Version:
Peer reviewed version

Origin of Efficient Inverted Non-Fullerene Organic Solar Cells: Enhancement of Charge Extraction and Suppression of Bimolecular Recombination Enabled by Augmented Internal Electric Field

Yiwen Wang,[a] *Bo Wu,*[a] *Zhenghui Wu,*[a] *Zhaojue Lan,*[a] *Yongfang Li,*[b,c] *Maojie Zhang,*[b,*] *and Furong Zhu*[a,*]

[a]Department of Physics, Institute of Advanced Material and Institute of Research and Continuing Education (Shenzhen), Hong Kong Baptist University, Kowloon Tong, NT, Hong Kong, China

[b]Laboratory of Advanced Optoelectronic Materials, College of Chemistry, Chemical Engineering and Materials Science, Soochow University, Suzhou 215123, China

[c]CAS Research/Education Center for Excellence in Molecular Sciences, CAS Key Laboratory of Organic Solids, Institute of Chemistry, Chinese Academy of Sciences, Beijing 100190, China

AUTHOR INFORMATION

Corresponding Author

*Email: frzhu@hkbu.edu.hk, mjzhang@suda.edu.cn

ABSTRACT: We report our effort to unraveling the origin of efficient operation of non-fullerene organic solar cells (OSCs), based on poly[4,8-bis(5-(2-ethylhexyl) thiophen-2-yl)benzo[1,2-b;4,5-b']dithioph-ene-2,6-diyl-alt-(4-(2-ethylhexyl)-3-fluorothieno[3, 4-b]thiophene-)-2-carboxylate-2-6-diyl)](PTB7-Th):3,9-bis(2-methylene-(3-(1,1-dicyanome thylene)-indanone))-5,5,11,11-tetrakis(4-hexylphenyl)-dithieno[2,3-d:2',3'-d']-s-indaceno [1,2-b:5,6-b']dithiophene (ITIC) blend system. The effects of buildup of space charges, charge extraction and bimolecular recombination processes on the performance and the stability of PTB7-Th:ITIC-based regular and reverse configuration OSCs are analyzed. It is found that the high performing inverted PTB7-Th:ITIC OSCs benefit from the combined effects of: (1) suppression of bimolecular recombination enabled by an augmented effective internal electric field, and (2) improvement of charge extraction by avoiding the holes passing through ITIC-rich region, which would otherwise occur in a regular configuration cell. The inverted PTB7-Th:ITIC OSCs possess a significant improvement in the cell stability, and a high power conversion efficiency of ~8.0%, which is >29% higher than that of an optimized regular configuration control cell (6.1%).

TOC GRAPHICS

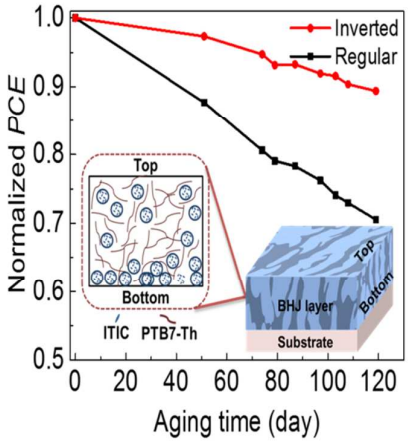

Organic solar cells (OSCs) are potentially attractive alternative to traditional inorganic photovoltaic devices. The development of solution processable OSCs has attracted great interests due to its low-cost non-vacuum process technology. The new polymer donor materials also exhibit a remarkable flexibility in tuning the material properties such as molecular weight, light absorption and energy band gap for new device concepts. OSCs based on blends of polymer and fullerene acceptors have enjoyed a dramatically development during the past decade. The power conversion efficiency (*PCE*) of >11.5% for fullerene-based OSCs has been reported.[1] However, fullerene acceptors still have some limitations for further improvement in cell performance, due to their weak absorption in the visible light spectrum, limited energy level tuning, challenging purification process and instable morphology of the polymer/fullerene blend layers.[2,3] The development of non-fullerene acceptor materials, e.g., fused-ring electron acceptor of 3,9-bis(2-methylene-(3-(1,1-dicyanomethylene)-indanone))-5,5,11,11-tetrakis(4-hexylphenyl)-dithieno[2,3-d:2',3'-d']-s-indaceno[1,2-b:5,6-b']dithiophene (ITIC), has attracted increasing attention for application in OSCs, due to the advantages of their tunable electronic properties, high absorption characteristics over the visible light region, lower lowest unoccupied molecular orbital (LUMO) and highest occupied molecular orbital (HOMO) energy levels, excellent miscibility with polymer donors,[4-8] and solution-fabrication capability towards large area low-cost flexible OSCs. For example, *PCE* of >12.2% for non-fullerene-based OSCs with an inverted cell structure has been reported,[9] demonstrating the exciting potential of non-fullerene OSCs for efficient organic photovoltaics.

OSCs can be formed using a regular configuration and an inverted structure, as illustrated in **Figure 1**. A stack of organic functional materials is sandwiched between a pair of anode and cathode. The photo-generated electrons and holes in the organic bulk heterojunction (BHJ) are drifted towards the cathode and anode under an effective internal electric field, which depends on the external load (bias) and the built-in potential in the cell. Apart from the choice of the donor/acceptor blend systems and the morphology of the organic active layer, device architecture also plays an important role involving in the processes of exciton generation, exciton dissociation, carrier transport, charge recombination, charge collection, and thereby the *PCE* and stability of OSCs. To date, the high performing non-fullerene OSCs with inverted device architecture are typically adopted, e.g., having a polymer donor: ITIC acceptor BHJ sandwiched between a front transparent cathode and a rear anode.[6-13] However, the advantages on suppression of bimolecular recombination and enhancement of charge extraction, which underpin the optimal cell performance and operational stability of the inverted non-fullerene OSCs have not yet been studied systemically.

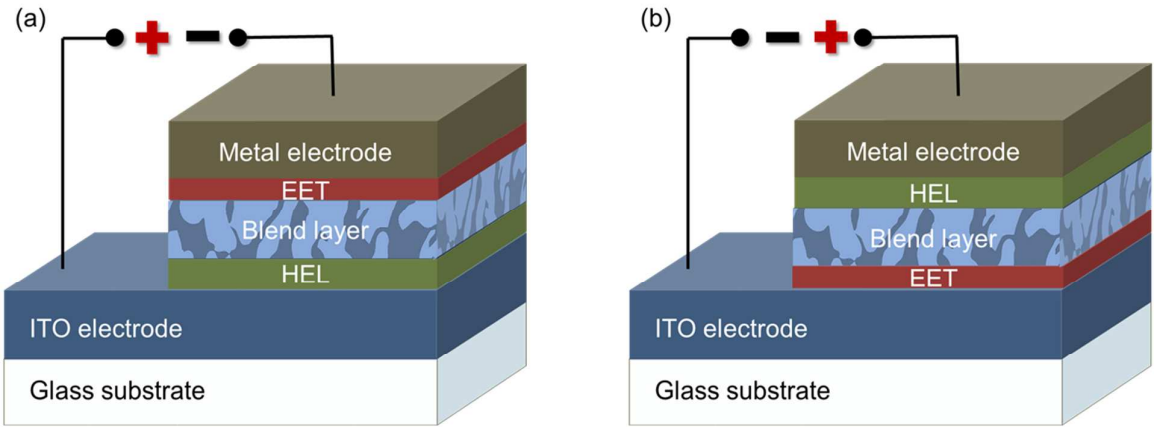

Figure 1. Schematic cross-sectional views of (a) a regular and (b) an inverted configuration OSCs, a pair of an electron extraction layer (EEL) and hole extraction layer (HEL) are used to assist in charge extraction.

In this work, we show that the inverted non-fullerene OSCs, based on poly[4,8-bis(5-(2-ethylhexyl)thiophen-2-yl)benzo[1,2-b;4,5-b']dithioph-ene-2,6-diyl-alt-(4-(2-ethylhexyl)-3-fluorothieno[3,4-b]thiophene-)-2-carboxylate-2-6-diyl)] (PTB7-Th): ITIC blend system, allow the efficient operation through simultaneous suppression of bimolecular recombination and improvement of charge extraction, enabled by an augmented effective internal electric field. The charge transport properties in PTB7-Th:ITIC BHJ were investigated using space-charge-limited current (SCLC) measurement. The effects of buildup of space charges, charge extraction and bimolecular recombination processes on the performance and the stability of the PTB7-Th:ITIC OSCs with a regular and an inverted configurations are analyzed using a combination of the transient photocurrent (TPC) and light intensity-dependent current density–voltage (*J–V*) characteristics. X-ray photoelectron spectroscopy (XPS) measurements reveal that there exists a donor/acceptor vertical phase separation in the PTB7-Th:ITIC blend layer, with an obvious ITIC-rich region present at the bottom of the BHJ. It is shown that the high performing inverted PTB7-Th:ITIC OSCs benefits from the combined effects of: (1) suppression of bimolecular recombination enabled by an augmented effective internal electric field, and (2) improvement of charge extraction by avoiding the holes passing through the ITIC-rich region, which would otherwise occur in the regular configuration cell. The inverted PTB7-Th:ITIC OSCs possess a dawdling degradation behavior and a *PCE* of ~8.0%, which is >29% higher than that of a control regular OSC (6.1%).

The thicknesses of the PTB7-Th:ITIC active layers in two sets of reverse and regular

configuration OSCs were optimized for achieving high *PCE*. The *J–V* characteristics measured for different reverse and regular configuration OSCs are shown in **Figure S1** and **Figure S2** in Supporting Information (SI), and the cell parameters are summarized in **Table S1** and **Table S2** in SI. *J–V* characteristics and incident photon to converted current efficiency (*IPCE*) spectra measured for the optimized inverted and regular OSCs are plotted in **Figure 2**. Compared to the performance of regular OSCs, the inverted PTB7-TH:ITIC OSCs possess obvious advantages, with increases in open circuit voltage (V_{OC}) from 0.82 V to 0.83 V, short circuit density (J_{SC}) from 13.33 mA/cm^2 to 14.58 mA/cm^2 and fill factor (*FF*) from 55.78% to 65.23% respectively, leading to an overall 29% increase in *PCE* from 6.10% (regular cell) to 7.89% (inverted cell). The evident enhancements in J_{SC} and *FF*, shown in **Figure 2(a)**, are the primary factors contributing to the superior performance of the inverted devices. The results in **Figure 2** show clearly that inverted OSCs possess enhanced charge collection efficiency and favorable photo-generated carrier transport properties.

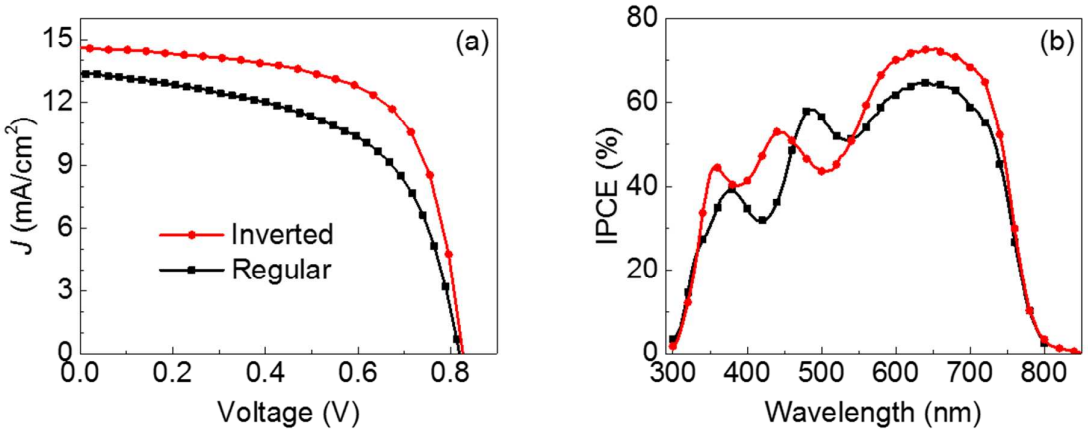

Figure 2. (a) *J*−*V* characteristics and (b) *IPCE* spectra measured for the inverted and the regular configuration PTB7-Th:ITIC OSCs.

The $J-V$ and characteristics and the *IPCE* spectra shown in **Figure 2**, measured for both sets of the inverted and regular configuration OSCs, are the average of more than 20 devices, fabricated using the identical process conditions. The variation in the resulting cell parameters obtained for the respective sets of the inverted and regular configuration OSCs is typically within an error range of <5%. The standard deviations of these cell parameters are given in **Table 1**. The inverted OSCs have a lower series resistance (R_S) of 6.54 Ω and a higher shunt resistance (R_{SH}) of 911.07 Ω as compared to R_S of 11.76 Ω and R_{SH} of 343.81 Ω measured for an optimized regular OSC. The dark *J–V* characteristics (**Figure S3** in SI) also illustrate that the inverted OSCs have a lower leakage current density. *IPCE* characteristics provide the information of light absorption in the active region contributing to exciton generation and external quantum efficiency of the devices. OSCs with an inverted configuration also exhibited an improved *IPCE* in almost the whole spectrum region, demonstrating an enhancement in the charge collection. A summary of device parameters obtained for both types of the PTB7-Th:ITIC OSCs is listed in **Table 1**.

Table 1. A summary of cell parameters measured for the inverted and regular configuration PTB7-Th:ITIC OSCs measured at AM1.5G of 100 mW/cm^2, the values of J_{SC} and *PCE* are calibrated using *IPCE* measurements.

Cell configuration	*PCE* (%)	J_{SC} (mA/cm^2)	*FF* (%)	V_{OC} (V)	R_S (Ω·cm^2)	R_{SH} (Ω·cm^2)
Inverted	7.89±0.13	14.58±0.07	65.23±0.13	0.83±0.01	6.54±0.34	911.07±16.92
Regular	6.10±0.11	13.33±0.05	55.78±0.28	0.82±0.00	11.76±0.89	343.81±1.93

Space Charge Buildup

To further study the charge transport in both types of OSCs, SCLC technique was used to calculate the electron mobility (μ_e) and hole mobility (μ_h) in the PTB7-Th:ITIC blend

system. The electron-only device of ITO/ZnO/PTB7-Th:ITIC/LiF/Al, and the hole-only device of ITO/PEDOT:PSS/PTB7-Th:ITIC/Au were prepared for the SCLC measurements. The $J^{0.5}$–V characteristics measured for the electron-only device under reverse bias and hole-only device under the forward bias are plotted in **Figure 3**. The $J^{0.5}$–V characteristics over the voltage region of >4 V is used for analyzing the SCLC charge-carrier mobility of the single-carrier devices. Although a linear regime in the single-carrier device also is seen at the low voltage region, it reflects the combination of drift and diffusion of charge carriers due to the rearrangement of the electric field inside the devices.[14,15] The electron mobility calculated by SCLC is 1.6×10^{-5} $cm^2V^{-1}s^{-1}$, while the hole mobility is 4.8×10^{-5} $cm^2V^{-1}s^{-1}$, showing an unbalanced charge transport ($\mu_h/\mu_e = 3$) between the electrons and the holes in the PTB7-Th:ITIC blend system. The buildup of the space charges also induces a decrease in the effective internal potential across the BHJ, leading to an increase in the related carrier recombination losses, and thereby deteriorating the device performance.[16]

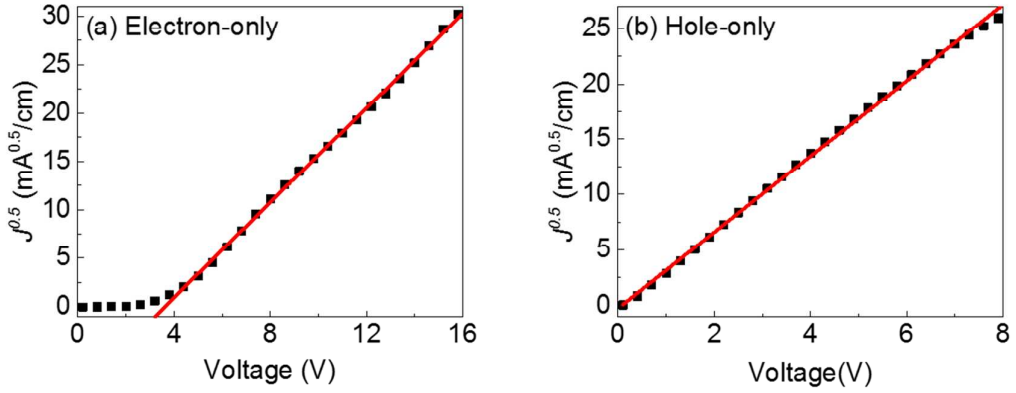

Figure 3. $J^{0.5}$–V characteristics obtained for (a) electron-only and (b) hole-only devices.

The $J^{0.5}-V$ characteristics measured for the electron- and hole-only devices under the forward

and reverse biases (**Figure S4** in SI) are compared. The value of μ_e derived from the electron-only device under the forward bias is in the range of 10^{-6} $cm^2V^{-1}s^{-1}$, which is about an order of magnitude lower than the one obtained for the electron-only device measured under the reverse bias. The difference in μ_e derived from the $J^{0.5}-V$ characteristics, measured for electron-only under the reverse and forward biases, suggests that the electrons can be injected (or extracted) easier when the electron-only device was measured under a reverse bias, implying the presence of an ITIC-rich region at the bottom and a polymer-rich region near the top of the active layer. SCLC measurements for the hole-only device further support this prediction. The value of μ_h measured for the hole-only devices under the reverse bias is in the order of 10^{-6} $cm^2V^{-1}s^{-1}$, which is lower than the one obtained for the device measured under the forward bias (~10^{-5} $cm^2V^{-1}s^{-1}$). The bias polarity dependent charge injection and extraction behaviors seen in the $J^{0.5}-V$ characteristics of the single-carrier devices measured under the forward and reverse biases (**Figure S4** in SI) reflect the formation of an inhomogeneous vertical distribution of donor and acceptor in the BHJ active layer. Therefore, it is expected that the buildup of space charges is closely associated with the imbalance of charge transport in the blend layer.

FF is sensitive to the presence of the space charges in the organic BHJ.[17] The buildup of the space charges also leads to the poor charge extraction. Thus, light intensity-dependent *FF* characteristics of both inverted and regular PTB7-Th:ITIC OSCs were measured and are plotted in **Figure 4**. The *FF* of inverted cells under different intensities of the incident light are always larger than that of the regular ones, implying that the inverted OSCs have a more

efficient charge collection probability due to a high effective internal electric field. *FF* of the inverted OSCs increases with decrease in light intensity, suggesting reduced bimolecular recombination (light-dependent recombination) probability due to the low density of photo-generated charge carriers. For regular configuration OSCs, the lower *FF* values were observed, showing a slower change in light intensity, caused by the inefficient charge collection efficiency.

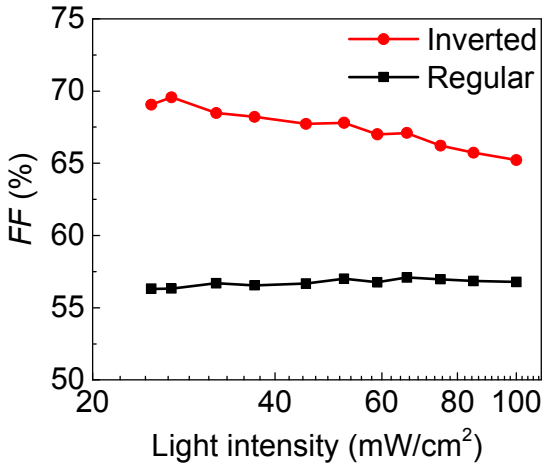

Figure 4. *FF–light intensity* characteristics measured for both an inverted and a regular PTB7-Th:ITIC OSCs.

TPC measurement is a technique to study the dynamics of the photo-generated carriers with a time scale of ~10 ns in electronic devices. The details of TPC measurement are described in the previous work.[18,19] The transient photocurrent can be calculated by:

$$I_{TPC} = I_L - I_D, \quad (1)$$

where I_L and I_D are the transient photocurrent and the dark current measured for the devices at same bias. The transient photocurrents measured for both types of OSCs as a function of the transient time, shown in **Figure 5**, are associated with the photo-generated carriers drift with

the effective internal electric field (E_{eff})[16,17] The effective internal potential (V_{eff}) across the organic BHJ is:

$$V_{eff} = V_0 - V_a. \quad (2)$$

E_{eff} is a function of the built-in potential (V_0), the external bias (V_a) and the thickness of the active layer (d), i.e.:

$$E_{eff} = (V_0 - V_a)/d. \quad (3)$$

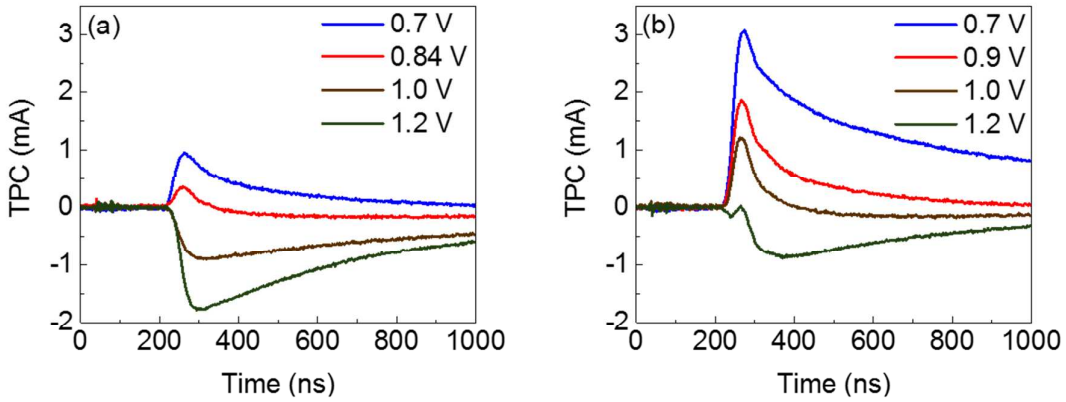

Figure 5. Transient photocurrents measured for (a) a regular and (b) an inverted PTB7-Th:ITIC OSCs at different biases.

The transient photocurrent I_{TPC}, formed under the effective internal electric field E_{eff}, can be offset by applying an opposite external bias on devices. The actual values of the built-in potential (V_0) in the OSCs can be examined by adjusting V_a to compensate V_0, i.e., tuning I_{TPC} approaching to zero in the absence of effective internal electric field. As shown in **Figure 5(a)**, I_{TPC} of the regular OSCs approaches to zero at an external bias of ~0.84 V, which corresponds to the actual built-in potential in the regular OSCs. Likewise, the built-in potential obtained for the inverted OSCs is ~1.0 V, as indicated in **Figure 5(b)**. The TPC results reveal clearly that the inverted PTB7-Th:ITIC OSCs possess a higher built-in potential

than that in a regular configuration OSC, made with an identical PTB7-Th:ITIC blend system. The optimized inverted OSCs have an active layer thickness of 80 nm, and that for the optimal of a regular cell is 100 nm (**Figure S1** and **Figure S2** in SI). According to **Equation 3**, the higher built-in potential coupled with a thinner active layer thickness (d) would result in a larger effective internal electric field E_{eff} in the inverted PTB7-Th:ITIC OSCs as compared to that in the regular cells. Therefore, it is expected that the inverted OSCs allow suppressing charge recombination loss, and thereby facilitating the photo-generated charge carriers being swept out efficiently under a higher effective internal electric field.

Charge Collection Efficiency and Recombination

Charge recombination and charge collection in solar cells are competing processes and are dependent on the effective internal electric field.[19] The recombination of the photo-generated charge carriers in OSCs mainly includes the bimolecular recombination and geminate recombination or trap-assisted recombination. The trap-assisted recombination takes place when the photo-generated electrons (holes) are captured by the traps and then recombined with the separated holes (electrons) in the BHJ layer. The bimolecular recombination is a non-geminate recombination loss process.

The behaviors of light intensity-dependence for both inverted and regular PTB7-Th:ITIC OSCs were measured. The results show that J_{SC} follows a power law dependence on light intensity, e.g.: $J_{sc} \propto I^{\beta}$, and V_{OC} varies logarithmically ($\ln I$) with light intensity, e.g.:

$V_{OC} \sim \left[(1-2)\cdot\frac{kT}{q}\right]\cdot \ln I$ (**Equation S12** and **Equation S15,** derivation of V_{OC}-ln$I$ expression is given in SI), respectively. The J_{SC} and V_{OC} as a function of light intensity, plotted in double logarithmic scales, are shown in **Figure 6(a) and Figure 6(b)**, respectively. Linear fittings also are given in **Figure 6**. From **Figure 6(a)**, it is seen that the value of the exponent β obtained for the inverted OSC is 1.0 and that for the regular cells is 0.96. The exponent β in the power law dependence of the photocurrent on light intensity is a good indication of photo-generation and extraction in the OSCs. It approaches to the unit when all the photo-generated carriers escape prior to recombination.

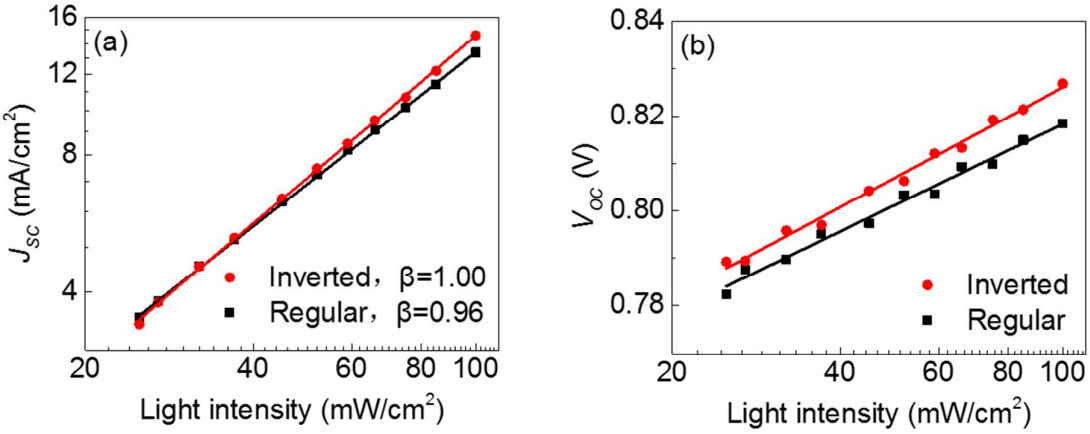

Figure 6. (a) J_{SC}–light intensity and (b) V_{OC}–light intensity characteristics measured for both an inverted and a regular PTB7-Th:ITIC OSCs.

The exponent less than 1.0 is due to different loss mechanisms, e.g., the buildup of space charges,[19] charge recombination,[20] and imbalanced hole-electron mobility in the cells.[21] The understanding on charge recombination in the inverted and regular PTB7-Th:ITIC OSCs can be further improved by analyzing their V_{OC}–light intensity characteristics. Because there is no current generated at the open circuit condition, therefore, the bimolecular recombination processes in the OSCs can be examined for the cells operated near V_{OC}. The slop of the

V_{OC}–ln$I$ plot approaches to $\frac{kT}{q}$ (**Equation S12** in SI) if the bimolecular recombination is the dominating recombination mechanism. The slope of the V_{OC}–ln$I$ plot changes to $2 \cdot \frac{kT}{q}$ (**Equation S15** in SI) for the condition when charge recombination loss is typically seen in the conventional inorganic solar cells. The slopes of the V_{OC}–ln$I$ plots obtained for the inverted and regular PTB7-Th:ITIC OSCs, shown in **Figure 6(b)**, are close to $\frac{kT}{q}$, suggesting that bimolecular recombination losses become significant in the OSCs as V_a approaches to V_{OC}. Reduction in bimolecular recombination loss is important for performance enhancement of PTB7-Th:ITIC OSCs.

Light intensity-dependent $J-V$ characteristics are a useful technique to analyze different charge recombination processes in the cells. The double logarithmic plots of $J_{ph}-I$ characteristics measured for the regular and inverted OSCs are shown in **Figure 7**. The power law dependence of J_{ph} on I can be observed. Photocurrent density J_{ph} is defined by the following equation:

$$J_{ph} = J - J_D, \quad (4)$$

where J is the current density measured under illumination, and J_D is the current density measured in the dark condition. As discussed in the previous work,[19,22] $J_{ph} \propto I^{\alpha}$, the exponent α approaches to unit, when almost all the photo-generated charge carriers are extracted prior to recombination. Less efficient charge transport and charge extraction in the OSCs will give rise to a smaller α value.

In **Figure 7**, it is seen that a high power exponent α of 1.0 for inverted PTB7-Th:ITIC OSCs

is obtained over the broad effective internal potential range from 0.88 – 0.13 V, e.g., corresponding to cells being operated at the short circuit (V_{eff} =0.88 V), maximum power output (V_{eff} =0.22 V) and near open circuit (V_{eff} =0.13 V) conditions. This indicates that the photo-carriers generated in the inverted PTB7-Th:ITIC OSCs can be swept out efficiently prior to recombination, resulting in a higher photocurrent density as shown in **Figure 2(a)**. The power exponent α obtained for the regular configuration OSCs decreases with the effective internal potential, with smaller values of 0.95 at short circuit (V_{eff} =0.88 V), 0.80 at maximum power output (V_{eff} =0.22 V) and 0.64 near open circuit (V_{eff} =0.22V) conditions. It is clear that the charge transport and charge collection in the regular PTB7-Th:ITIC OSCs are less efficient. Inefficient charge extraction leads to the buildup of space charges that gives rise to higher bimolecular recombination, and thereby leading to a lower power exponent. The results shown in **Figure 7** reveal that the buildup of space charges and the subsequent bimolecular charge recombination occurring in the regular configuration OSCs can be greatly suppressed in the inverted OSCs.

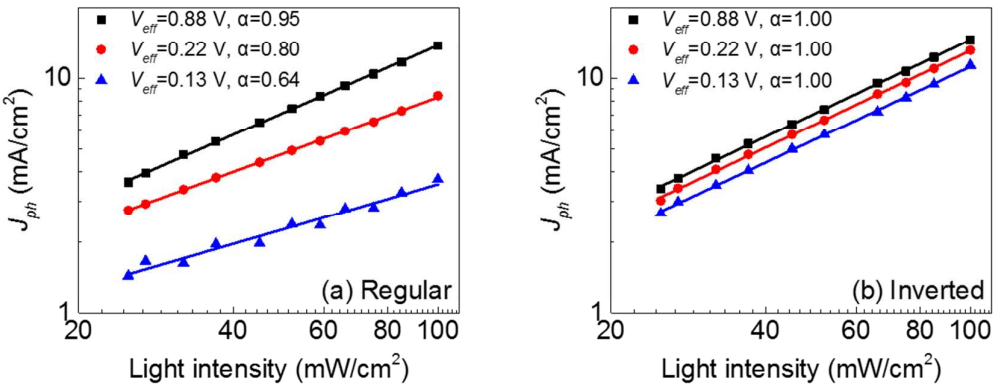

Figure 7. Double logarithmic plots of photocurrent density as a function of light intensity measured for (a) a regular configuration and (b) an inverted PTB7-Th:ITIC OSCs under different effective voltages.

Charge collection characteristics (J_{ph}–V_{eff}) in the PTB7-Th:ITIC-based inverted and regular configuration OSCs are plotted in **Figure 8**. The charge recombination is a function of V_{eff} the in the cells, e.g., the first order (monomolecular) recombination, dominated recombination processes occurred at the short circuit condition (V_{eff}=V_0), gradually shifts to the second order (bimolecular) recombination processes in OSCs operated near the open circuit state (V_{eff} =0 V).[23] From short circuit point to the maximum power output (V_{eff} >0.22 V), monomolecular recombination dominates the total loss, when V_{eff} <0.22 V, bimolecular recombination becomes significant. Charge collection efficiency (η_{cc}) describes the total losses of charge carriers during the charge transport in the BHJ active layer and the charge extraction at the anode/organic and organic/cathode interfaces under different V_{eff}. Bimolecular recombination is the most important factor limiting η_{cc} in OSCs over the low V_{eff} range, which can be calculated by:

$$\eta_{cc}\left(I, V_{eff}\right) = \frac{J_{ph}(I,V_{eff})}{J_{ph,sat}(I)} \quad (5)$$

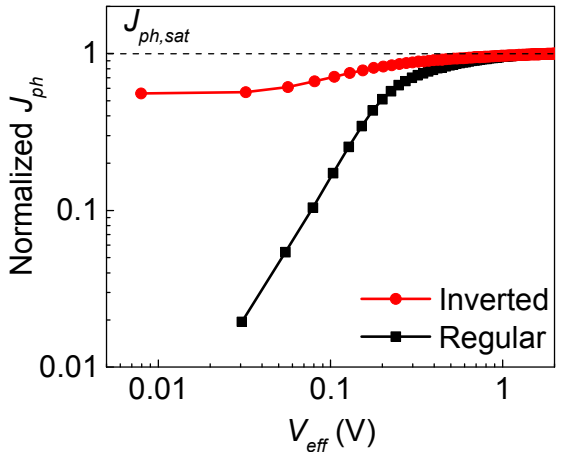

Figure 8. J_{ph}–V_{eff} characteristics illustrating the difference in charge collection probability of an inverted and a regular configuration PTB7-Th:ITIC OSCs.

In **Figure 8**, the η_{cc} probability of the regular PTB7-Th OSCs is always lower than that of the

inverted cells, due to an obvious increase in bimolecular recombination loss. For regular cell, η_{cc} decreases from 58% at maximum power output (V_{eff} =0.22 V) to 25% at V_{OC} point (V_{eff} =0.13 V), while only a 10% drop in η_{cc} from 84% (at maximum power output) to 75% (at V_{OC} point) occurs in the inverted devices. The results confirm that the inverted cells possess more efficient charge collection efficiency due to the suppression of the bimolecular recombination loss.

To analyze the miscibility of the ITIC with PTB7-Th in the BHJ, the vertical compositional distribution of the PTB7-Th and ITIC in the blend layer was analyzed using XPS measurements. XPS is a surface-sensitive spectroscopic technique for measurement and quantitative analysis of elemental composition in the films. Wide scans of XPS spectra measured for the individual PTB7-Th (black spectrum) and ITIC films (red spectrum) are plotted in **Figure 9(a)**. The C_{1s}, S_{2s} and S_{2p} XPS peaks at the binding energies of 284.6 eV, 228 eV and 164 eV are observed in the XPS spectra measured for both PTB7-Th and ITIC films. F_{1s}, peaked at 688 eV, is seen only in the PTB7-Th XPS spectrum, while the N_{1s} XPS peak, observed at a binding energy of 400 eV, is unique to ITIC acceptor, as shown in the ITIC XPS spectrum. Therefore, F_{1s} (PTB7-Th) and N_{1s} (ITIC) XPS peaks are used to examine the vertical compositional distribution of the polymer (PTB7-Th) and the non-fullerene acceptor (ITIC) in the blend layer. Wide scans of XPS spectra measured for the top (black spectrum) and the bottom (red spectrum) surfaces of the two identical PTB7-Th:ITIC blend films are shown in **Figure 9(b)**. F_{1s} and N_{1s} XPS peaks are seen in the XPS spectra measured for the top and the bottom surfaces of the blend layers. The N_{1s} (from ITIC) XPS spectra

measured for the top and bottom surfaces of the PTB7-Th:ITIC blend films are plotted in **Figure 9(c),** and F_{1s} (from PTB7-Th) XPS spectra measured for the top and bottom sides of the same blend layers are shown in **Figure 9(d)**.

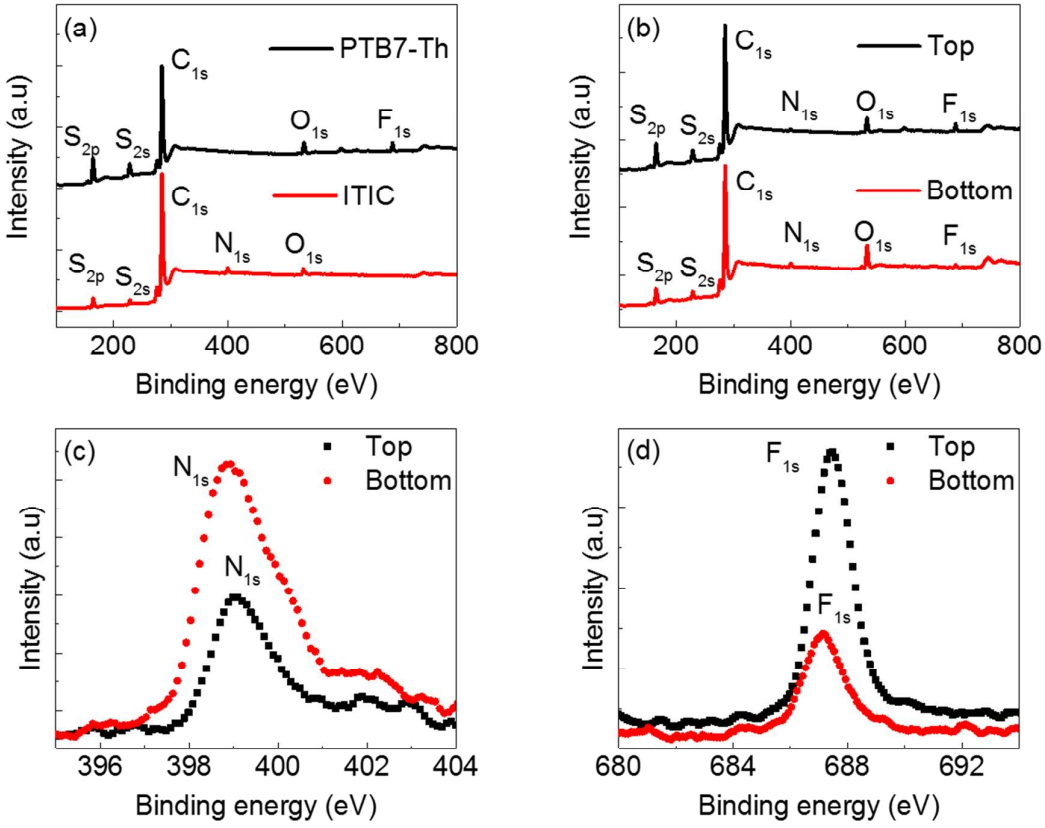

Figure 9. XPS spectra measured for (a) the individual PTB7-Th and ITIC films, (b) the top and bottom surfaces of the PTB7-Th:ITIC blend layers. (c) N_{1s} (from ITIC) and (d) F_{1s} (from PTB7-Th) XPS spectra measured for the top and bottom surfaces of the PTB7-Th:ITIC blend film.

It is seen clearly that there is a dramatic change in the intensity of N_{1s} and F_{1s} XPS spectra measured for the top and the bottom surfaces of the same blend layers, indicating a non-uniform distribution of the PTB7-Th and ITIC in the vertical direction in the blend layer. A combination of a strong intensity of N_{1s} XPS peak (from ITIC) and a relative weak F_{1s} XPS

peak (from PTB7-Th) is observed from the bottom side of the PTB7-TH:ITIC blend layer. In contrast, a combination of a weak intensity of N_{1s} XPS peak (from ITIC) and a strong F_{1s} XPS peak (from PTB7-Th) is observed from the top surface of the blend layer. The changes in the relative compositional ratio of ITIC to PTB7-Th (ITIC/PTB7-Th ratio) on the top and bottom surfaces of the PTB7-Th:ITIC blend layers can be analyzed using the area ratios of N_{1s}/C_{1s}, N_{1s}/S_{2p}, F_{1s}/C_{1s}, F_{1s}/S_{2p} XPS spectra. The results are summarized in **Table 2**. There is an obvious increase in the ITIC/PTB7-Th ratio obtained from the top surface (0.46) to that of the bottom surface (3.65) of the blend layer. XPS results support the analyses made with the $J^{0.5}-V$ characteristics of the single-carrier devices, indicating that an inhomogeneous distribution of the ITIC and PTB7-Th occurs in the blend layer, forming an ITIC-rich region towards the bottom of the blend layer.

Table 2. The area ratios of XPS spectra N_{1S}/C_{1S}, N_{1S}/S_{2P}, F_{1S}/C_{1S}, F_{1S}/S_{2P} and the relative compositional ratio of ITIC to PTB7-Th obtained from the top and bottom surfaces of the PTB7-Th:ITIC blend films.

Blend surface	N_{1S}/C_{1S}	N_{1S}/S_{2P}	F_{1S}/C_{1S}	F_{1S}/S_{2P}	ITIC/PTB7-Th ratio
Top	0.009	0.081	0.019	0.180	0.46
Bottom	0.021	0.337	0.006	0.089	3.65

The relative compositional ratios of ITIC to PTB7-Th calculated for the top surfaces of different PTB7-Th:ITIC blend films deposited on ZnO, PEDOT:PSS and glass (**Table S3** in SI) are very similar (~0.5). They are consistently lower than that of the ITIC/PTB7-Th ratio (~3.65) measured for the bottom side of the blend film, peeled off from the one deposited on glass, implying that the PTB7-Th:ITIC active layers in the inverted and regular configuration

OSCs have similar inhomogeneous vertical phase separation behavior. The schematic drawing illustrating the vertical phase separation of ITIC and PTB7-Th in the BHJ is shown in **Figure 10**. It is seen that the aggregation of ITIC at the bottom of active layer is not favorable for the efficient operation of the regular configuration OSCs, as the holes need to pass through the ITIC-rich region before they are collected by the anode, giving rise a higher charge recombination. For inverted OSCs, the electrons are collected by the bottom electrode (ITO cathode), avoiding extraction of the holes via an ITIC-rich region, which would otherwise occur in the regular configuration cell.

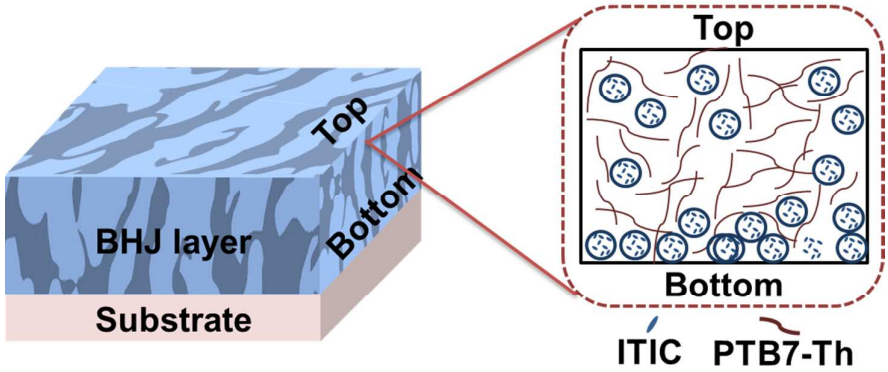

Figure 10. Schematic drawing illustrating the presence of a vertical phase separation between PTB7-Th and ITIC in the active layer, forming an ITIC-rich region towards the bottom of the PTB7-Th:ITIC blend layer.

Stability of the OSCs

The aging test of the inverted and regular PTB7-Th:ITIC OSCs was conducted in the glove box. Both types of OSCs were kept in the dark at room temperature. To prevent the degradation due to the possible interaction between the OSCs and the residual chemical vapors in the glovebox, the cells were encapsulated for the aging tests. The cell parameters of

V_{OC}, J_{SC}, *FF* and *PCE* measured for the inverted and regular configuration OSCs as a function of aging time are shown in **Figure S5**. The normalized V_{OC}, J_{SC}, *FF* and *PCE* measured for the inverted and regular configuration OSCs as a function of aging time are shown in **Figure 11**. The inverted OSCs experienced a much slower degradation in J_{SC} and *FF*, and thereby a slower decrease in *PCE* as compared to that of the regular OSCs. For inverted OSCs, there is a 2.6% drop in J_{SC}, 7% drop in *FF* and an 11% decrease in *PCE* after 120 days. While for the regular cells, a fast reduction in the J_{SC}, *FF* and *PCE* are observed during the aging test, having 7.7% drop in J_{SC}, 23% drop in *FF* and 29% drop in *PCE*, respectively.

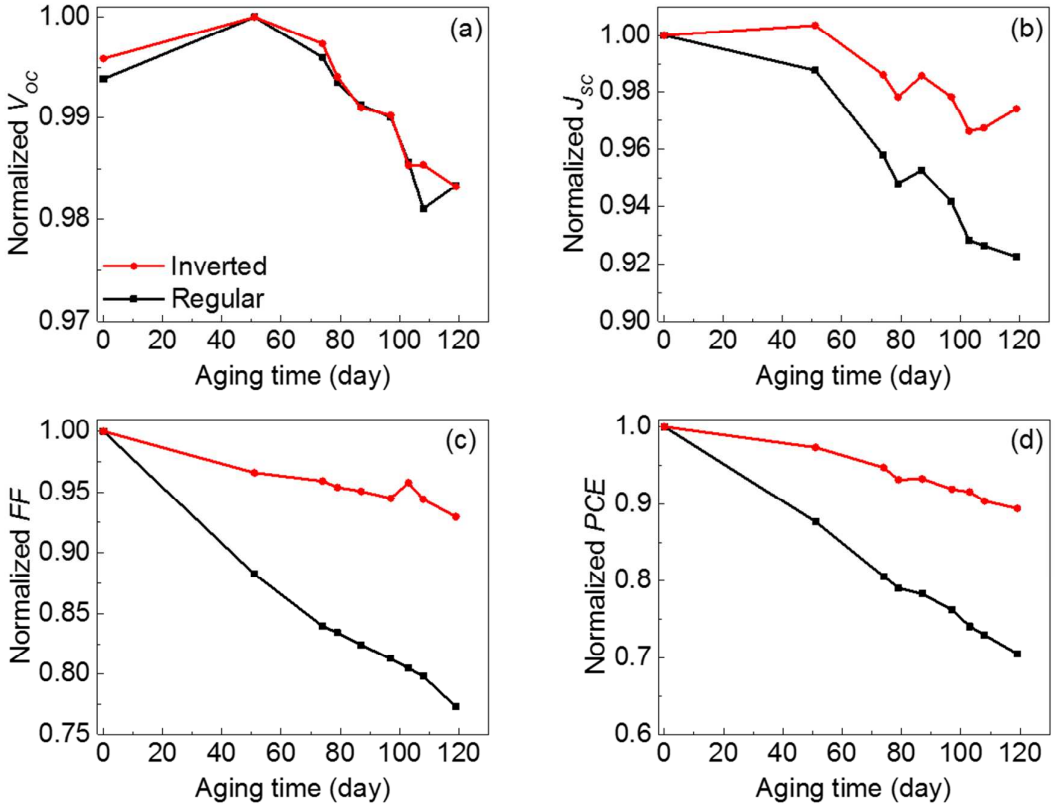

Figure 11. Normalized (a) V_{OC} (b) J_{SC} (c) *FF* (d) *PCE* as a function of the aging time, measured for the inverted and regular PTB7-Th:ITIC OSCs over a period of 120 days.

The normalized charge collection efficiency of the reverse and regular configuration OSCs,

operated at two different effective internal potentials of 0.22 V (maximum power output) and 0.13 V (near V_{OC} condition), as a function of aging time is plotted in **Figure 12**. It is shown that the regular configuration OSCs undergo a much fast deterioration in the η_{cc} as compared to the inverted OSCs during the same aging test. The analyses on charge collection agree with the degradation behavior of J_{SC} and FF shown in **Figure 11**. A close look at the charge collection efficiency for cells operated at $V_{eff} = 0.22\,V$ (maximum power output) shown in **Figure 12(a)**, the inverted OSCs display an 11% drop in η_{cc}, which is much smaller than that of the regular configuration OSCs (36%) after 120 day aging test. The bimolecular recombination losses become significant in the cells operated near V_{OC} condition, e.g., at $V_{eff} = 0.13\,V$. The η_{cc} value of regular OSCs declines by 48% after 120 days, which is much higher than that of the inverted devices (27%). Improved charge extraction in the cells indicates the efficient charge transport and reduced loss to the charge recombination.

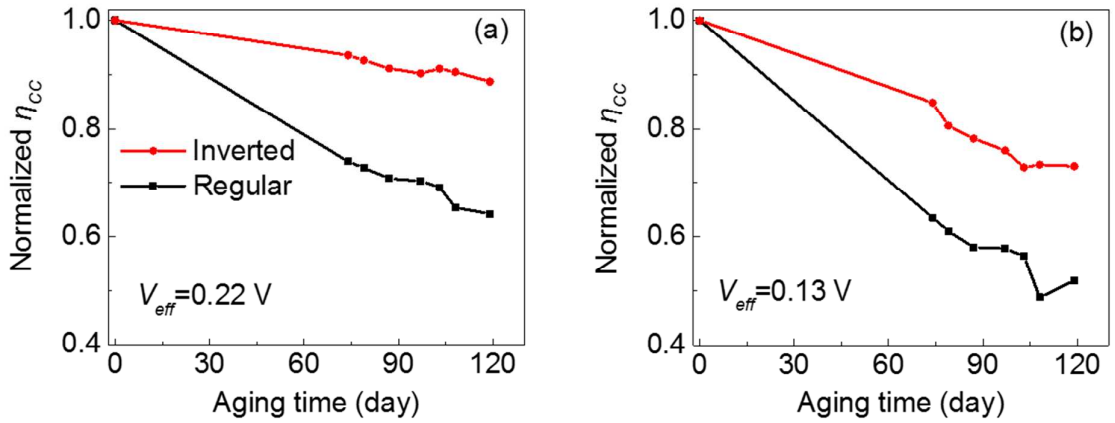

Figure 12. Normalized charge collection efficiency as a function of the aging time, measured for the inverted and regular PTB7-Th:ITIC OSCs at (a) $V_{eff} = 0.22\,V$ (corresponding to maximum power output), and (b) $V_{eff} = 0.13\,V$ (approach to open circuit condition).

Based on the TPC, light intensity-dependent *J–V* characteristics and the XPS measurements,

we conclude that the reverse device configuration benefits the efficient operation of PTB7-Th:ITIC OSCs in two ways: (1) suppression of bimolecular recombination enabled by a greater effective internal electric field, and (2) improvement of charge extraction by avoiding the holes passing through an ITIC-rich region. The combined effects also enable the inverted PTB7-Th:ITIC OSCs possessing a dawdling degradation process.

In summary, the effects of space charge buildup, charge extraction and bimolecular recombination processes on the performance of PTB7-Th:ITIC OSCs are analyzed. It is found that the origin of high performing inverted PTB7-Th:ITIC OSCs is mainly due to the suppression of bimolecular recombination and the enhancement of charge extraction probability, enabled by a greater effective internal electric field in the inverted cells. The combined effects also lead to a dawdling cell degradation process.

Experimental Section

Devices Fabrication and Characterizations: Non-fullerene-based OSCs were fabricated using ITO/glass substrates with a sheet resistance of 10 Ω/square. The substrates were cleaned by ultrasonication sequentially with dilute detergent solution, deionized water, acetone and isopropanol for 30 min each. For fabrication of the inverted OSCs, the ITO/glass substrates were directly transferred to the glove-box with O_2 and H_2O levels <0.1 ppm, zinc oxide layer (ZnO) was then spin-coated on the substrate. The synthesis of solution processable ZnO nanoparticles is described in a previous work.[24] Polymer blend of PTB7-Th (1 Material) and

ITIC in a weight ratio of 1:1.3 was fully dissolved in chlorobenzene solution at 60°C before use. A layer of active PTB7-Th:ITIC layer was spin-coated on the ZnO/ITO surface using different rotation speeds for attaining optimal cell performance. The samples were then transferred to the adjacent vacuum chamber with a base pressure of $<5.0 \times 10^{-4}$ Pa for deposition of a 2 nm thick molybdenum oxide (MoO_3) interlayer and a 100 nm thick Ag top electrode. The inverted OSCs have a cell structure of glass/ITO/ZnO (10 nm)/PTB7-Th:ITIC (80 nm)/MoO_3 (2 nm)/Ag (100 nm). Regular configuration OSCs with a structure of glass/ITO/PEDOT:PSS (30 nm)/PTB7-Th:ITIC (100 nm)/ ZnO (20 nm)/Ag (100 nm) were also fabricated for comparison study. Both types of the OSCs have an identical active area of 3.0 mm×3.0 mm, defined by the overlap area of the anode and the cathode. *In situ J–V* characteristics of OSCs were measured under AM1.5G illumination of 100 mw/cm^2 using a SAN-EI Electric XEC-301S solar simulator, attached to the N_2-purged glove box. Light intensity of the solar simulator was calibrated using a single crystalline silicon detector (with a KG-5 filter) to minimize the spectral mismatch. After the *in situ J–V* characteristic and *IPCE* measurements, devices were encapsulated and removed from the glove box for the *ex situ* TPC measurement.

Transient Photocurrent Measurements: Transient photocurrents measured for the reverse and regular configuration OSCs were recorded using an oscilloscope (Tektronix MDO3052 Mixed Domain Oscilloscope), illuminated using a pulsed Nd:YAG laser with the wavelength of 532 nm and a pulse duration of <5 ns at different forward biases. The details of the TPC measurement set-up are described in a previous work.[18]

X-ray Photoelectron Spectroscopy Analyses: In situ XPS measurements were carried out using a VG ESCALAB 220i-XL surface analysis system, equipped with a monochromatic Al Kα source providing photons with 1486.6 eV for XPS measurements. The ITIC/PTB7-Th ratio on the top surface of the PTB7-Th:ITIC blend film was analyzed by measuring the elemental composition of the film coated on the silicon substrate. To study the composition of the PTB7-Th and ITIC on the bottom surface of a blend layer, the PTB7-Th:ITIC blend film was deposited on glass substrate with an ultrathin LiF buffer layer, the PTB7-Th:ITIC blend layer was then removed from the glass substrate in deionized water, the film was then turned upside down and transferred to the silicon substrate for XPS measurements.

ACKNOWLEDGMENT

This work was financially supported by the Research Grants Council of Hong Kong Special Administrative Region, China, General Research Fund (12303114, 12302817), Hong Kong Baptist University Inter-institutional Collaborative Research Scheme (RC-ICRS/15-16/04) and Shenzhen Peacock Plan (KQTD20140630110339343).

ASSOCIATED CONTENT

Supporting Information

Theoretical derivation of V_{OC}–ln$I$ expression, performance of reverse and regular configuration OSCs with different active layer thicknesses, as well as the stability results of the optimized reverse and regular configuration OSCs supplied as Supporting Information.

AUTHOR INFORMATION

Corresponding Author

*E-mail: frzhu@hkbu.edu.hk, mjzhang@suda.edu.cn

Notes

The authors declare no competing financial interests

REFERENCES

(1) Zhao, J. B.; Li, Y. K.; Yang, G. F.; Jiang, K.; Lin, H. R.; Ade, H.; Ma, W.; Yan, H. Efficient Organic Solar Cells Processed from Hydrocarbon Solvents. *Nat. Energy* **2016**, *1*, 15027.

(2) Guerrero, A.; Heidari, H.; Ripolles, T. S.; Kovalenko, A.; Pfannmöller, M.; Bals, S.; Kauffmann, L. D.; Bisquert, J.; Garcia-Belmonte, G. Shelf Life Degradation of Bulk Heterojunction Solar Cells: Intrinsic Evolution of Charge Transfer Complex. *Adv. Energy Mater.* **2014**, *4*, 1401997.

(3) Chen, C.P.; Huang, C. Y.; Chuang, S. C. Highly Thermal Stable and Efficient Organic Photovoltaic Cells with Crosslinked Networks Appending Open-Cage Fullerenes as Additives. *Adv. Funct. Mater.* **2015,** *25,* 207–213.

(4) Lin, Y. Z.; Wang, J. Y.; Zhang, Z. G.; Bai, H.T.; Li, Y. F.; Zhu, D. B.; Zhan, X. W. An Electron Acceptor Challenging Fullerenes for Efficient Polymer Solar Cells. *Adv. Mater.* **2015**, *27*, 1170-1174.

(5) Lin, Y. Z.; Zhan, X. W. Designing Efficient Non-Fullerene Acceptors by Tailoring Extended Fused-Rings with Electron-Deficient Groups. *Adv. Energy Mater.* **2015**, *5*, 1501063.

(6) Dai, S. X.; Zhao, F. W.; Zhang, Q. Q.; Lau, T. K.; Li, T. F.; Liu, K.; Ling, Q. D.; Wang, C.

R.; Lu, X. H.; You, W.; Zhan, X. W. Fused Nonacyclic Electron Acceptors for Efficient Polymer Solar Cells. *J. Am. Chem. Soc.* **2017**, *139*, 1336–1343.

(7) Wang, W.; Yan, C. Q.; Lau, T. K.; Wang, J. Y.; Liu, K.; Fan, Y.; Lu, X. H.; Zhan, X. W. Fused Hexacyclic Nonfullerene Acceptor with Strong NearInfrared Absorption for Semitransparent Organic Solar Cells with 9.77% Effciency. *Adv. Mater.* **2017**, *29*, 1701308.

(8) Wang, J. Y.; Wang, W.; Wang, X. H.; Wu, Y.; Zhang, Q. Q.; Yan, C. Q.; Ma, W.; You, W.; Zhan, X. W. Enhancing Performance of Nonfullerene Acceptors via Side-Chain Conjugation Strategy. *Adv. Mater.* **2017**, *29*, 1702125.

(9) Li, S. S.; Ye, L.; Zhao, W. C.; Zhang, S. Q.; Mukherjee, S.; Ade, H.; Hou, J. H. Energy-Level Modulation of Small-Molecule Electron Acceptors to Achieve over 12% Efficiency in Polymer Solar Cells. *Adv. Mater.* **2016**, *28*, 9423–9429.

(10) Lin, Y. Z.; He, Q.; Zhao, F. W.; Huo, L. J.; Mai, J. Q.; Lu, X. H.; Su, C. J.; Li, T. F.; Wang, J. Y.; Zhu, J. S. et al. A Facile Planar Fused-Ring Electron Acceptor for As-Cast Polymer Solar Cells with 8.71% Efficiency. *J. Am. Chem. Soc.* **2016**, *138*, 2973-2976.

(11) Lin, Y. Z.; Zhao, F. W.; He, Q.; Huo, L. J.; Wu, Y.; Parker, T. C.; Ma, W.; Sun, Y. M.; Wang, C. R.; Zhu, D. B. et al. A High-Performance Electron Acceptor with Thienyl Side Chains for Organic Photovoltaics. *J. Am. Chem. Soc.* **2016**, *138*, 4955–4961.

(12) Zhao, W. C.; Qian, D. P.; Zhang, S. Q.; Li, S. S.; Inganäs, O.; Gao, F.; Hou, J. H. Fullerene-Free Polymer Solar Cells with over 11% Efficiency and Excellent Thermal Stability *Adv. Mater.* **2016**, *28*, 4734–4739.

(13) Ye, L.; Zhao, W. C.; Li, S. S.; Mukherjee, S.; Carpenter, J. H.; Awartani, O.; Jiao, X. C.; Hou, J. H.; Ade, H. High-Efficiency Nonfullerene Organic Solar Cells: Critical Factors that

Affect Complex Multi-Length Scale Morphology and Device Performance. *Adv. Energy Mater*. **2017**, *7*, 1602000.

(14) Kirchartz, T. Influence of Diffusion on Space-charge-limited Current Measurements in Organic Semiconductors. *Beilstein J. Nanotechnol.* **2013**, *4*, 180–188.

(15) Röhr, J. A. Kirchartz, T. Nelson, J. On the Correct Interpretation of the Low Voltage Regime in Intrinsic Single-carrier Devices. *J. Phys. Condens. Matter* **2017**, *29*, 205901.

(16) Kotlarski, J. D.; Blom, P. W. M. Impact of Unbalanced Charge Transport on the Efficiency of Normal and Inverted Solar Cells. *Appl. Phys. Lett.* **2012**, *100*, 013306.

(17) Qi, B. Y.; Wang, J. Z. Fill Factor in Organic Solar Cells. *Phys. Chem. Chem. Phys.* **2013**, *15*, 8972.

(18) Wu, B.; Wu, Z. H.; Tam, H. L.; Zhu, F. R. Contrary Interfacial Exciton Dissociation at Metal/Organic Interface in Regular and Reverse Configuration Organic Solar Cells. *Appl. Phys. Lett*. **2014**, *105*, 103302.

(19) Wu, Z. H.; Wu, B. H.; Tam, H. L.; Zhu, F. R. An Insight on Oxide Interlayer in Organic Solar Cells: From Light Absorption and Charge Collection Perspectives. *Org. Electron.* **2016**, *31*, 266-272.

(20) Cowan, S. R.; Roy, A.; Heeger, A. J. Recombination in Polymer-Fullerene Bulk Heterojunction Solar Cells. *Phys. Rev. B* **2010**, *82*, 245207.

(21) Rose, A. Concepts in Photoconductivity and Allied Problems, Wiley, New York, USA **1963**.

(22) Wu, B.; Wu, Z. H.; Yang, Q. Y.; Zhu, F. R.; Ng, T. W.; Lee, C. S.; Cheung, S. H.; So, S. K. Improvement of Charge Collection and Performance Reproducibility in Inverted Organic

Solar Cells by Suppression of ZnO Subgap States. *ACS Appl. Mater. Interfaces* **2016**, *8*, 14717-14724.

(23) Firdaus, Y.; Vandenplas, E.; Khetubol, A.; Cheyns, D.; Gehlhaar, R.; Van. Der. Auweraer, M. Charge Transport and Recombination in P3HT:PbS Solar Cells. *J. Appl. Phys.* **2015**, *117*, 095503.

(24) Liu, H. X.; Wu, Z. H.; Hu, J. Q.; Song, Q. L.; Wu, B.; Tam, H. L.; Yang, Q. Y.; Choi, W. H.; Zhu, F. R. Efficient and Ultraviolet Durable Inverted Organic Solar Cells based on an Aluminum-doped Zinc Oxide Transparent Cathode. *Appl. Phys. Lett*. **2013**, *103*, 043309.